AGU ADVANCING EARTH AND SPACE SCIENCE

Geophysical Research Letters®

RESEARCH LETTER
10.1029/2022GL102348

Time of Emergence for Altimetry-Based Significant Wave Height Changes in the North Atlantic

Antoine Hochet[1], Guillaume Dodet[1], Florian Sévellec[1], Marie-Noëlle Bouin[1,2], Anindita Patra[1], and Fabrice Ardhuin[1]

[1]Laboratoire d'Océanographie Physique et Spatiale, University Brest CNRS IRD Ifremer, Brest, France, [2]CNRM, Université de Toulouse, Météo-France, CNRS, Toulouse, France

Key Points:

- Altimeter based significant wave height trends in the North Atlantic (NA) are largely dominated by internal variability
- Forced significant wave height changes in the NA will only be detectable in altimeter data after 2050

Supporting Information:

Supporting Information may be found in the online version of this article.

Correspondence to:

A. Hochet,
ahochet@ifremer.fr

Citation:

Hochet, A., Dodet, G., Sévellec, F., Bouin, M.-N., Patra, A., & Ardhuin, F. (2023). Time of emergence for altimetry-based significant wave height changes in the North Atlantic. *Geophysical Research Letters*, *50*, e2022GL102348. https://doi.org/10.1029/2022GL102348

Received 5 DEC 2022
Accepted 22 MAR 2023

Abstract Satellite observations of significant wave height (H_s) have recently reached 30 years of continuous record. Is this length sufficient to detect the effect of anthropogenically forced climate change on wave height trends? Wave height decadal variability is influenced by a combination of internal variability and forced variability caused by both anthropogenic and natural forcing. Using a statistical model to derive H_s from sea level pressure field and exploiting ERA-5 reanalysis data as well as 80 members of the Community Earth System Model v2 large ensemble, we show that, over the North Atlantic (NA), altimetry-based H_s trends are mostly caused by internal variability. This suggests that H_s changes computed over the satellite era are not yet controlled by anthropogenic climate change. Starting from 1993, the date of emergence, defined as the date when the forced signal becomes dominant over the internal variability, is later than 2050 for H_s in the NA.

Plain Language Summary Satellite observations of significant wave height will soon reach 30 years of continuous record. Changes in significant wave height over this period can either be attributed to both anthropogenic or "natural" climate forcing or to the intrinsic variability of the climate system. In this article, we show that the intrinsic variability effect largely dominates the significant wave height changes in the North Atlantic (NA) over the 30 years of satellite observations. We further estimate that the significant wave height changes associated with anthropogenically forced climate change will become dominant over those due to the intrinsic variability after 2050 in most of the NA region.

1. Introduction

For the end of 2022, 30 years of uninterrupted multi-platform altimeter records of global significant wave height will become available. The 30 years represent the minimum duration required for computing climatological standards following the World Meteorological Organization recommendation (WMO, 2015). In recent years, several authors (e.g., Dodet et al., 2020; Ribal & Young, 2019; Timmermans et al., 2020; Young & Ribal, 2019; Young et al., 2011) have computed the trends in both the mean and extreme significant wave height (H_s) using calibrated data from multi-mission altimeter records. Young and Ribal (2019) found weak positive trends for mean H_s, of the order of 0.3 cm yr^{-1} for the 1985–2018 period and larger positive trends for the 90th percentile of H_s in the mid to high latitudes of the North Atlantic (NA). We investigate what is the contribution of the forced, anthropogenic climate change on these observed trends. Since the atmosphere exhibits internal variability on decadal to multi-decadal time scales, which is comparable to the duration of the current satellite era, these trends could be the signature of the internal variability and therefore be completely different in a few years or decades when more data will be available. Nonetheless, with sufficiently long recording length, the magnitude of the trends from the anthropogenic signal should eventually become larger than the trends caused by the internal variability, as expected for other climate variables (Hawkins & Sutton, 2009).

Using the comparison between a control run (Ctrl) with pre-industrial greenhouse gases concentration and a forced simulation (Forc) with future "business as usual" emission scenario (RCP8.5) for the 2010–2060 period, Dobrynin et al. (2015) found detectable climate change signal in the 2010–2020 decade in the NA and elsewhere. This detection is based on the comparison of the levels of inter-annual to decadal variability in Ctrl and in Forc. If the Forc variability exceeds the range of the Ctrl variability defined by means of a probability density function fitted through an ensemble of subsampled segments from the Ctrl simulation, then the anthropogenic climate change is said to be detectable. However the fact that the externally forced climate change is detectable in the H_s variability when compared to a pre-industrial run does not inform us about the amplitude of the modification

since a given date. Here our goal is different: starting from the beginning of the altimeter era, we want to assess the date by which the amplitudes of the anthropogenic trends become larger than the amplitude of the trends linked to other sources of variability and therefore become detectable in satellite altimetry climate data record. This approach is similar to the "signal to noise" approach that has been used for instance in Hawkins and Sutton (2011) to infer the uncertainty linked with the internal variability (referred as the noise) in various climate variables such as the temperature or the precipitation rate. In the remainder of this article, we will use the term forced variability to refer to the variability forced supposedly by the increase of greenhouse gases due to anthropogenic forcing and use the term internal variability to refer to the difference between the total and forced variability. Note that the forced variability has other contributors, such as variations of solar irradiance or volcanic activity. However, for long-term trends their impacts remain weak in comparison (Suckling et al., 2017, for instance).

This study focuses on the NA because it is a region of intense maritime traffic, numerous marine energy project and new engineering infrastructures that necessitates an accurate understanding of its wave climate variability. Moreover, numerous studies have demonstrated the link between the NA winter H_s variability and the winter Sea Level Pressure (SLP) variability over the same region (Bacon & Carter, 1993; Dodet et al., 2010; Gulev et al., 1998; Hochet et al., 2021; Kushnir et al., 1997; Shimura et al., 2013; Woolf, 2002). In particular, a large part of the H_s variability is believed to be correlated with the North Atlantic Oscillation (NAO) winter index (Woolf, 2002). Wang et al. (2012) constructed a statistical model to link H_s and SLP using data from ERA-interim reanalysis (Dee et al., 2011) and used it to study the 20th century H_s trends. In this study, we will use the NA SLP/H_s relationship to link satellite era trends of H_s to decadal variability of SLP. Then, using a large ensemble of simulations from a climate model and using SLP to reconstruct H_s changes, we will decompose the H_s trends into forced and internal components. These two components will then be compared to derive a date of emergence (DoE) of H_s trends, which is the date by which this forced signal dominates the internal variability and thus becomes the leading cause of the H_s modification.

This article is organized as follows: in Section 2, the significant wave height trends are computed over different periods of time and compared. In Section 3, we derive and assess a statistical model to link SLP and H_s variabilities. In Section 4, outputs from a large ensemble simulation of a climate model are used to assess the role of the forced signal in the satellite altimetry H_s trends and to estimate its DoE. In Section 5, we conclude and discuss our results.

2. Winter H_s Trends in Reanalysis and Satellite Data

In this study, we focus on the January-February-March (JFM) months because the H_s inter-annual variability is stronger during these boreal winter months in the NA (Castelle et al., 2018; Dodet et al., 2010; Shimura et al., 2013; Woolf, 2002) which makes the SLP/H_s statistical relationship more robust. For conciseness, we drop the JFM prefix in what follows, except in figure captions. The H_s trends computed over the period 1993–2018, using the European Centre for Medium-Range Weather Forecasts ERA-5 reanalysis data (Hersbach et al., 2020) are shown in Figure 1 (panel a). The 1993–2018 period corresponds to the era of the multi-mission altimeter product (L4 monthly gridded data, version 1, Piollé et al., 2020) developed within the ESA Sea State Climate Change Initiative (CCI) project (Dodet et al., 2020). 5% significant negative values, down to −3.3 cm yr^{-1} are found in the Norwegian Sea while positive values are found in the western part of the Mediterranean Sea (up to 3 cm yr^{-1}), off the U.S. East Coast, and at low latitudes with weaker values around 1 cm yr^{-1}. The same H_s trends computed using data from the CCI multi-mission altimeter product are also shown in Figure 1 (panel b) for comparison. Results are qualitatively similar to the trends obtained from ERA-5 data, with positive values in the western Mediterranean Sea and off the U.S. East Coast and negative values in the Norwegian Sea. However, the CCI data set gives 5% significant values almost everywhere at low latitudes, south of 20°N, whereas the ERA-5 data set low latitudes significant trends are only located along the Brazilian north coast. Since simulations of H_s decadal variability may vary between wave model hindcast and reanalysis (Erikson et al., 2022), we have compared the JFM H_s trends in 8 different data sets of the NA (Figures S1 and S2 in Supporting Information S1). Results show that in this region, the agreement between the different data sets is high.

The ERA-5 H_s trends computed for the 1950–2018 period (Figure 1, panel c) are very different from the 1993–2018 trends both in pattern and magnitude with values approximately three times as small as the satellite-era trends. The 1950–2018 H_s trends are positive in the eastern high latitudes of the NA, with magnitude of the order of 1 cm s^{-1} and are negative (but not significant) around 40°N. In particular, trends are non significant in the western Mediterranean Sea, positive in the Norwegian Sea and weakly positive off the U.S. East Coast. This is different from the trend computed over the 1993–2018 period. This indicates that there is a strong variability in the winter H_s field on a time scale close to the duration of the current satellite era and that trends computed over

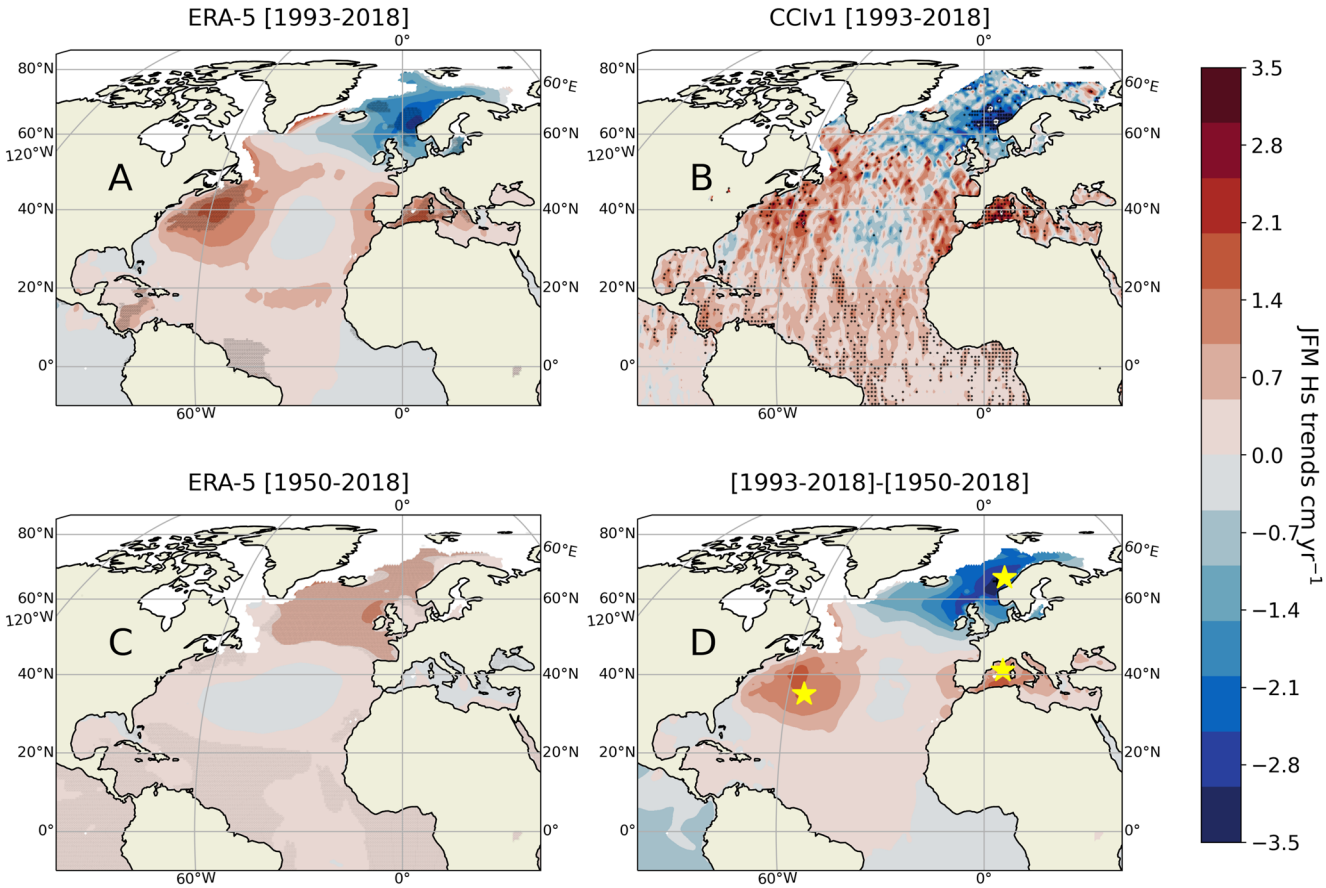

Figure 1. JFM H_s trends cm yr^{-1} for the 1993–2018 period obtained from the ERA-5 data set (panel a) and the CCI v1 data set (panel b). The JFM H_s trends (cm yr^{-1}) for the 1950–2018 period obtained from ERA-5. 5% significant trends are marked with a black dot (panel c). Difference between the JFM H_s trend (cm yr^{-1}) computed for the 1993–2018 and 1950–2018 periods (panel d). Yellow stars represent specific locations study in more details in Section 3.

the 1993–2018 period are very likely to change when computed over longer period when more data will become available. In Panel d of Figure 1 we show the difference between the 1993–2018 and 1950–2018 trends computed with ERA-5 reanalysis. Because of its larger magnitude, the 1993–2018 trend dominates the signal (giving a hint on the dominance of interdecadal variability over multidecadal one). In the following section, we focus our analysis in three locations (shown with three orange stars in Figure 1) where the 1993–2018 trends are the largest: the Norwegian Sea, the western Mediterranean Sea, and the sea off the U.S. East Coast.

3. Statistical Relationship Between H_s and SLP Variability

In this section, we first illustrate the strong relationship between the SLP variability and H_s variability by computing the correlation between the two fields for the three locations (indicated by the orange stars in Figure 1). We then take advantage of the well documented relationship between the SLP variability and H_s variability over the NA (Hochet et al., 2021; Shimura et al., 2013; Woolf, 2002) to develop a simple statistical model that links the H_s variability to the SLP variability. This statistical relationship will then be used in the following section to reconstruct the H_s trends from the SLP outputs of a climate model ensemble.

3.1. Correlation Between JFM H_s and JFM SLP

To illustrate the strong statistical relationship between SLP and H_s in the NA, we first compute the time correlation over the 1950–2018 period between detrended 2-dimensional SLP and detrended H_s timeseries located at each of the three selected locations (orange stars in Figure 1):

$$R_{SLP}^{H_s^l}(x,y) = \mathrm{corr}\left[\mathrm{SLP}(x,y,t), H_s^l(t)\right], \quad (1)$$

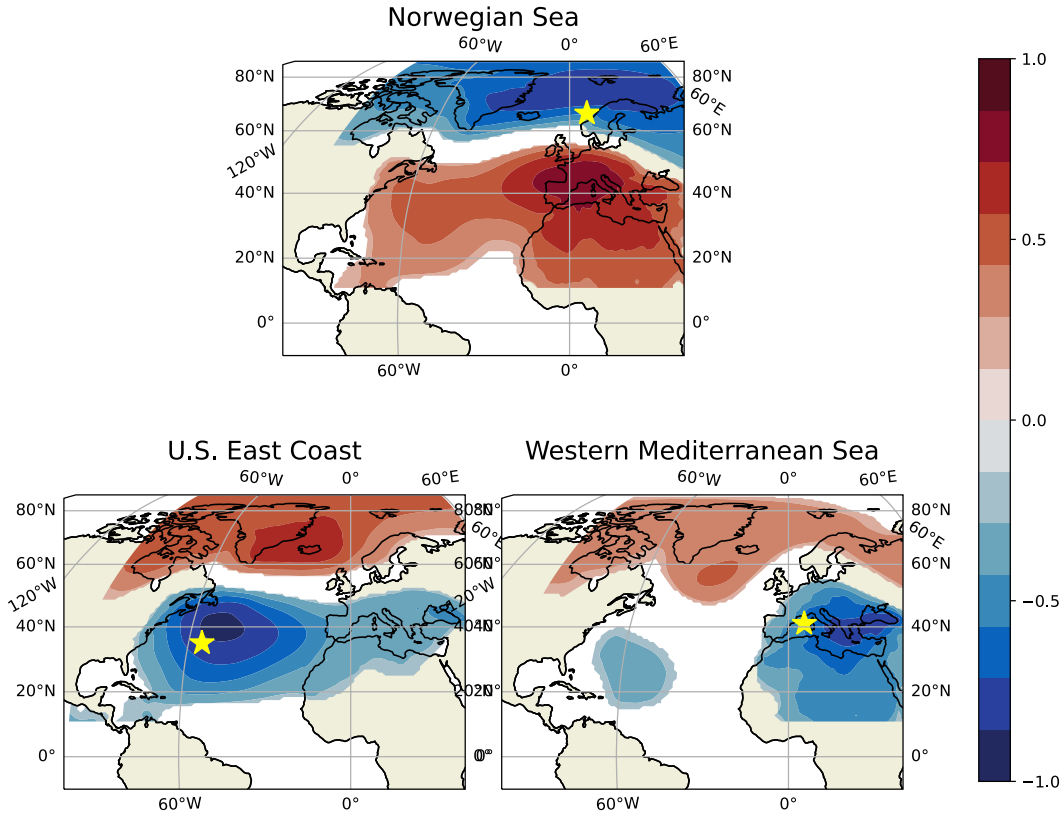

Figure 2. Time correlation between the time series of H_s in the Norwegian Sea region (top panel), Us East Coast region (bottom left panel), and Western Mediterranean (bottom right panel) and 2-dimensional SLP over the 1950–2018 period. The studied location is shown with yellow star of the corresponding panels. Only 5% significant values are shown.

where H_s^l is the timeseries of H_s at lth location, l = 1,2,3 is the index associated to the Norwegian Sea, Us East Coast, and Western Mediterranean location, respectively, and $R_{SLP}^{H_s^l}$ is the time correlation between the 2-dimensional SLP and H_s^l timeseries. This calculation is somehow similar to previous studies where the time correlation between H_s and the first PCs of the Northern Hemisphere SLP is computed (Hochet et al., 2021; Shimura et al., 2013; Woolf, 2002).

The significant wave height at the three locations is significantly correlated with SLP over most of the Atlantic basin (Figure 2), which indicates that the differences between the 1993–2018 H_s trend and the 1950–2018 trend at the three locations are associated with the basin-scale SLP variability. In the Norwegian Sea, H_s is associated to a SLP pattern that resembles a positive phase of the NAO pattern dipole but with a positive anomaly shifted to the east, above the Iberian Peninsula. The time correlation between H_s in this location and the main modes of atmospheric variability over the NA reveals that H_s variations are mainly controlled by the NAO and the Scandinavian index and to a lesser extent by the Eastern Atlantic Western Russia index (EAWR) (see Table S1 in Supporting Information S1). The SLP correlation pattern for the US East Coast region resembles a negative phase of the NAO pattern dipole but with a negative anomaly shifted to the western part of the Atlantic. Correlations with the main NA atmospheric variability indices confirms that H_s is negatively correlated with the NAO and reveals that it is also weakly positively correlated with the NINO3.4 index. The western Mediterranean region has a different H_s/SLP correlation pattern compared to the two previous locations, with a SLP center of action centered and localized above the Mediterranean Sea and a weaker opposite sign anomaly at high latitudes, above Greenland, Iceland, and the Scandinavian Peninsula. H_s in the Western Mediterranean region is negatively correlated by the EA (Eastern Atlantic index), and also negatively correlated with the NAO and the EAWR. These relationships between climate modes and H_s variations in these three locations are in agreement with descriptions from the literature (e.g., Trigo et al., 2008).

3.2. Statistical Model

To construct a statistical model to link variations in SLP and H_s, we start by decomposing the ERA-5 detrended SLP (i.e., SLP anomalies, SLPA) for the 1950–2018 period over the NA region into its principal components:

$$\mathrm{SLPA} = \sum_i \mathrm{EOF}_i(x, y)\mathrm{PC}_i(t), \tag{2}$$

where PC_i is the normalized time dependent principal component of mode i and EOF_i the corresponding spatial pattern of SLPA which satisfies:

$$\langle \mathrm{SLPA}|\mathrm{EOF}_i\rangle = \mathrm{PC}_i\langle \mathrm{EOF}_i|\mathrm{EOF}_i\rangle, \tag{3}$$

with

$$\langle A|B\rangle = \frac{1}{S}\int_S A(x, y)B(x, y)ds, \tag{4}$$

where S and ds are the total and unit surface areas, respectively. Note that because the Principal Components PCs have been normalized (i.e., is unit-less), the EOF are not normalized, that is, $\langle \mathrm{EOF}_i|\mathrm{EOF}_i\rangle \neq 1$. However EOFs are still forming an orthogonal basis so that $\langle \mathrm{EOF}_i|\mathrm{EOF}_i\rangle \neq 0$ and $\langle \mathrm{EOF}_i|\mathrm{EOF}_j\rangle = 0$ for $i \neq j$. Then, for each location of the NA, the detrended H_s anomaly is time-projected on the SLP principal components:

$$\beta_i(x, y) = \frac{1}{T}\int_T \mathrm{PC}_i(t)H_s(x, y, t)dt, \tag{5}$$

where T and dt are the total and unit times, respectively, and $\beta_i(x, y)$ is the time projection of $H_s(x, y, t)$ on $\mathrm{PC}_i(t)$. The reconstructed $\tilde{H}_s$ is obtained using:

$$\tilde{H}_s(x, y, t) = \sum_i \beta_i(x, y)\frac{\langle \mathrm{EOF}_i|\mathrm{SLPA}\rangle(t)}{\langle \mathrm{EOF}_i|\mathrm{EOF}_i\rangle}. \tag{6}$$

To assess this statistical reconstruction, we train the model using the ERA-5 SLP and H_s variability over the period 1950–1993 and then assess it using the 1993–2018 period. To train the model, the Principal components and associated EOFs of the 1950–1993 SLP are first computed following Equation 2. Then, the 1993–2018 H_s is projected on the Principal Components using Equation 5. H_s is finally reconstructed using Equation 6 with the ERA-5 SLP over the 1993–2018 period. To assess the reconstruction, we compute the time correlation between the ERA-5 H_s and $\tilde{H}_s$ (Figure S1 in Supporting Information S1). We find that the best results are obtained when 25 EOFs of SLP are used. The correlation is high (>0.75) almost everywhere and has a mean of 0.72 when non-significant values are excluded. Non significant correlations are mostly found at low latitudes and close to the western boundary of the basin. In the following section, we use the full period of ERA-5 (1950–2018) to train the statistical model which will be used to derive H_s from a large ensemble of climate simulations.

4. Signature of Anthropogenical Forcing on H_s Trends

In this section, the relative importance of the forced and internal variability in the reconstructed H_s trends is assessed using SLP outputs from a large ensemble of simulations of the Community Earth System Model version 2 (CESM2). The CESM2 Large Ensemble (LENS2) consists of 100 members at 1° spatial resolution covering the period 1850–2100 under Climate Model Intercomparison Project 6 historical (until 2015) and Shared Socioeconomic Pathways SSP3-7.0 (from 2015) as radiative forcing scenarios (Lehner et al., 2020). Here, we only use the 80 members that have been publicly released. These 80 members are each subject to identical external forcings and only differ by their initial conditions (Lehner et al., 2020). It is assumed that the average across a sufficient number of members removes the unphased sequences of internal variability and gives the model's response to external forcing (both internal and anthropogenic). It is worth noting that of these external forcings only the anthropogenically forced one corresponds to a sustain trend. Hence a sustained trend on the SLP response will be associated to it (and not to other, natural forcing). Using 40 members of the Community Climate System Model 3, Deser et al. (2012) considered SLP trends from 2005 to 2060 and argued that 20–30 members were necessary to accurately quantify the forced response. Similarly, using the Max Planck institute Grand Ensemble,

Maher et al. (2019) evaluate that 40–50 members are needed to robustly isolate the pattern of the forced trend in SLP. In wave climate study, the number of members considered is generally much smaller, for instance, Lemos et al. (2019) and Lemos et al. (2020) used respectively 4 and 7 members to decompose the wave field into forced and internal components. Casas-Prat et al. (2022) have investigated the H_s trends over the 1951–2010 period using a 100-member ensemble derived from an Atmospheric General Circulation Model (d4PDF ensemble Mizuta et al., 2017) and found that only 10 members were necessary to separate the forced and internal variabilities. However it is now well established that the ocean plays an important role in the interannual to multi-decadal variability of the climate system for instance through ENSO or the variability of the Atlantic Meridional Overturning Circulation. Thus, an atmospheric-only model might underestimate the level of low-frequency variability. We thus choose here to use a coupled climate model. Given the strong relationship between the SLP field and the significant wave height variability outlined in the previous section and in numerous previous studies (see Hochet et al., 2021, for a review of these studies), the number of members required to decompose the H_s into forced and internal variabilities should be similar to that required for the SLP field.

The number of members required to decompose the forced and internal components depends on the length of the trend considered. In the supporting information we show, using the NAO index, that for trends computed over a short period of time such as the 30 years of the altimeter era period, more than 50 members are required, while for longer trend periods, less members are required (Figure S4 in Supporting Information S1). Here, with 80 members we thus ensure that our decomposition of the forced and internal variability is robust. The drawback of such a large number of members is that it would be too computationally expensive to run a wave model on the outputs of the climate model. However, the statistical relationship between the SLP variability and H_s trends allows to use the SLP fields provided by climate models as a robust proxy for H_s variability. In this work we are interested in the order of magnitude of the time of emergence of the forced H_s signal and will use the H_s/SLP statistical relationship to infer this value from SLP outputs of the CESM LENS2.

4.1. Date of Emergence of H_s in the NA

In this subsection we assess the relative contribution of internal and forced H_s variability over the satellite altimetry era and longer time periods. More specifically, the goal is to give an estimation of the duration needed for the emergence of the anthropogenically forced trend from the residual internal variability, that is, the time of emergence (Giorgi & Bi, 2009; Nguyen et al., 2018). To this end, we take advantage of the correlation between H_s and the SLP variability outlined using ERA-5 data in the previous section to use the CESM LENS2 ensemble mean (EM) of the SLP to diagnose the EM and standard deviation of the H_s trends. For this purpose the EM of the reconstructed $H_s\left(\tilde{H}_s\right)$ can be obtained as:

$$\overline{\tilde{H}_s} = \frac{1}{N}\sum_{j=1}^{N}\tilde{H}_{sj}, \tag{7}$$

$$\widehat{\tilde{H}_s} = \sqrt{\frac{1}{N}\sum_{j=1}^{N}\left(\tilde{H}_{sj} - \overline{\tilde{H}_s}\right)^2}, \tag{8}$$

where $\tilde{H}_{sj}$ is the reconstructed H_s from individual member j and $N = 80$ is the total number of members.

The EM of the H_s trend over the 1993–2018 period increases with latitudes with values up to 0.6 cm yr^{-1} (panel a of Figure 4), positive values are found North of latitude 50°N while negative values are located South of this latitude. The magnitude and sign of the EM differs largely from the 1993–2018 H_s trends computed from the ERA-5 and satellite data sets (Figure 1). However the EM trend patterns is similar to that obtained by Casas-Prat et al. (2022) for the period 1951–2010 in the NA. The standard deviation of the reconstructed 1993–2018 H_s trends (panel b of Figure 3) also increases with latitude and have values up to 1.5 cm yr^{-1} North of 40°N. There, it is apparent that the standard deviation of the trends is larger than the EM trend, showing that, in this region, the internal variability dominates the forced signal for the 1993–2018 period. For each location, we compute the percentage of members that have the same sign has the 1993–2018 EM H_s trend (panel c of Figure 3). Maximum values are around 80% but are located at low latitudes in the Gulf of Mexico where the H_s trends are weak and where the statistical reconstruction is poor. North of 40°N, a mean percentage of 55% is obtained, which further suggest that the H_s trend sign of any single member is primarily controlled by the internal variability.

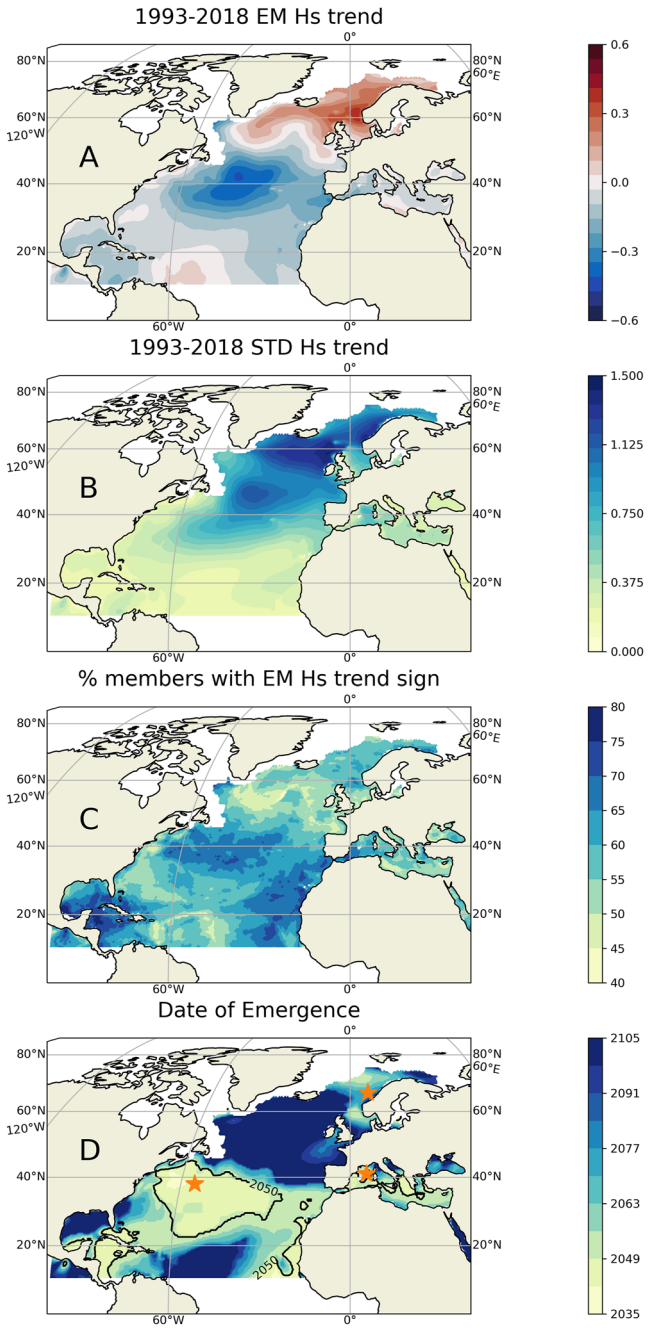

Figure 3. Panel (a) ensemble mean (EM) of the reconstructed H_s trend (in cm yr^{-1}) over the period 1993–2018, panel (b) standard deviation of the reconstructed H_s trend (cm yr^{-1}) over the same period. Panel (c) percentage of members with same 1993–2018 H_s trend sign as the ensemble mean. Panel (d) date of emergence of the reconstructed H_s forced trend. The date of emergence is as the date where the amplitude of the EM trend is equal to 1.64 times the standard deviation of individual member trend. The 2050 contour is shown in black. The three colored stars show the location of the studied time series.

We compute a DoE of the H_s trend that we define as the date for which the EM trend is 1.64 as large as the standard deviation of the trends. Assuming a Gaussian behavior, the 1.64 coefficient insures that there is only 5% of chance that the individual member H_s trend is opposite to that of the EM. Most of the NA has a DoE occurring later than 2050 (Panel c of Figure 3). Only a few regions have a DoE occurring earlier than 2050: the western part of the Mediterranean Sea, a region off the U.S. east coast and a region in the Gulf of Mexico. 95% of the members have spatial correlation between the reconstructed H_s trends and EM trend larger than 0.5 by 2060 (Figure S2 in Supporting Information S1). This inter-member consistency further confirms the limited influence of the internal variability for trends computed over such long period (1993–2060).

4.2. Decomposition of the Reconstructed H_s in the Three Locations of Interest

We now turn to the comparison of the trends in the three specific locations already discussed earlier (marked by orange stars in panel d of Figure 3). Writing α_j^{1993-t} the $\tilde{H}_{sj}$ as the trend from 1993 to time t, we define $\overline{\alpha^{1993-t}}$ and $\widehat{\alpha^{1993-t}}$ the EM and inter-member standard deviation of the trends, respectively, for the same period of time; where their relative values gives an estimation of the relative role of the forced and internal variability in setting the H_s trends. The results are very similar in the three regions (Figure 4): EM H_s trend $(\overline{\alpha})$ represents no more than 10%–15% of the standard deviation of the total trends when the end date is 2018. For this relatively short period of time, the sign of the total trend depends primarily on the phase of the internal variability and can either be positive or negative for all three regions. The red dots on the three panels show that the H_s trends obtained from ERA-5 data are at the maximum of the range of possible values given by the CESM2 ensemble. It is negative in the Norwegian Sea and positive in the two others regions (in agreement with the trends computed directly from ERA-5 H_s over the same period of time).

For the Norwegian Sea region, the sign of the EM trend is always positive for all period of times considered here while it is always negative for the two other regions. These signs are in agreement with the projected intensification of the positive phase of the NAO (Masson-Delmotte et al., 2021). The fact that the ERA-5 derived trends (red dots) have their sign opposite and their magnitude larger compared to that of the EM trend in the three regions further show that the satellite era trends are not dominated by the forced trends but rather by the internal variability. It also outlines that the effect of the internal variability on the H_s trends is currently (2022) possibly opposite to that of the forced signal. Thus the H_s trends computed over the satellite altimetry era cannot yet be interpreted as an estimate of the changes due to anthropogenic climate change. The DoE of the H_s trend is respectively 2060, 2050, and 2048 for the Norwegian sea, U.S. East Coast, and Western Mediterranean Sea locations. Therefore, at these three locations, approximately 30 more years of satellite data will be required to obtain a trend that can be safely attributed to the forced variability.

5. Discussion and Conclusion

In this study, we have shown that the winter-averaged (JFM) H_s significant trends computed over the satellite altimetry period (1993–2018) in the NA are associated with decadal variability of the SLP field. Using this

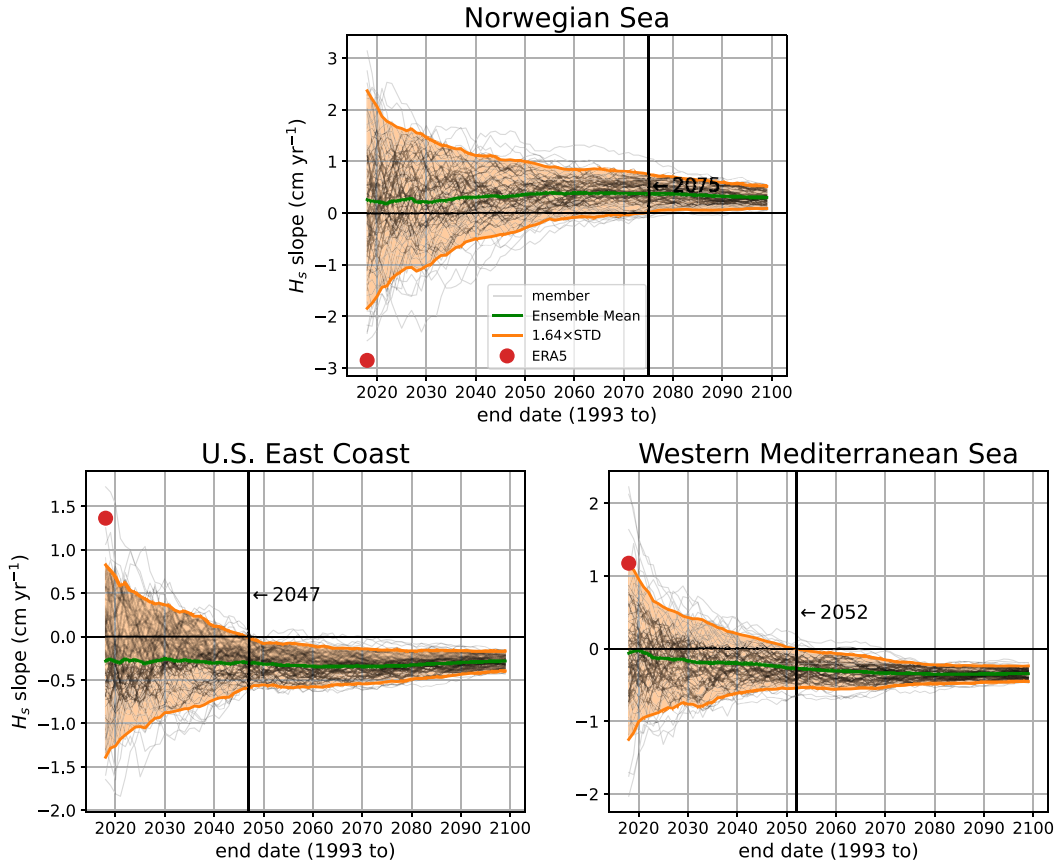

Figure 4. Trends of the reconstructed H_s slope for the 80 individual members of the CESM2 Large Ensemble starting from 1993 and as a function of the end date (2018–2100) for the three specific locations (orange star in panel d of Figure 3). Gray lines show individual member trend and green lines ensemble means. The area where 95% of individual trends have the same sign as the ensemble mean trend are shaded in orange (i.e., individual member are within the ensemble mean plus/minus 1.64 times the inter-member standard deviation). The vertical black line shows the date of emergence corresponding to the date where 95% of individual trends have the same sign (i.e., EM is equal to the 1.64 inter-member standard deviation). The red dots show the ERA-5 1993–2018 H_s trends computed at the locations.

statistical relationship between H_s and the SLP variability we then showed that the H_s trends can be decomposed into two parts: a forced contribution mainly linked on long-timescale to the increased radiative forcing and a contribution associated with the internal variability of the climate system (Deser et al., 2012). Starting from 1993, this decomposition shows that the H_s trends associated with the radiative forcing are currently (i.e., in 2022) much smaller than the trends associated with the internal variability. Thus, H_s trends computed from the satellite altimetry or over the same period in ERA-5 mainly reflect the internal variability rather than the forced climate change and are thus very different from the trends computed on the CESM LENS2 EM (inferring the forced component). An important result of this study is therefore that it is currently not possible to estimate the changes in H_s due to anthropogenic forcing without the use of an ensemble of simulation to remove the effect of the internal variability. This implies that it is currently impossible to estimate anthropogenically forced H_s trend from observations alone. Further, we showed that the date when both parts will become of similar magnitude depends on the region. Defining a DoE as the date when 95% of individual members have the same sign than the forced component, we find that it ranges from 2050 in some parts of the NA to later than 2100. It suggests that H_s trends currently computed from satellite altimetry are mostly due to internal variability and are likely to become significantly different from their current values in the upcoming years and decades.

A limitation of our study concerns the limited representation of the atmospheric multi-decadal variability in climate models. Indeed, a number of recent studies have shown that climate models significantly underestimate the amplitude of multi-decadal NAO, jet stream variability or sea surface temperature (Kim et al., 2018; Kravtsov, 2017; Sévellec & Drijfhout, 2019; Simpson et al., 2018). If the amplitude of the internal multi-decadal

variability is in fact larger than simulated by climate models, the DoE for H_s would occur even later than what was shown in this study (Figures 4 and 3). Moreover, this study employs a single forcing scenario (SSP3-7.0) and the uncertainty associated with the forcing scenario choice has been shown to mainly affect the long term projections (i.e., around 2100, Lehner et al., 2020). A different choice of forcing scenario might thus slightly modify the DoE. However, we believe that the use of the intermediate forcing scenario SSP3-7.0 ensure that the order of magnitude of the emergence date is correct.

A second limitation concerns the use of SLP as a proxy for the decomposition of H_s. Indeed, it is possible that the current statistical relationship between the SLP and H_s (computed here over the 1950–2018 period) will evolve and thus lead to bias in the reconstructed H_s. However given that a large number of members is required to decompose the SLP (and by extent the H_s) and that H_s is not simulated in climate models it would be computationally very expensive to run a wave model over the 80 members for a 110-year period. Hence, we believe that our approach based on the SLP decomposition is sufficient to provide first order information on the relative importance of the internal and forced variability and on the time of emergence of the forced signal. The low correlation between the reconstructed JFM H_s and the ERA-5 JFM H_s found at latitudes lower than 20°N (see Figure S3 in Supporting Information S1) are probably due to the influence of other modes of atmospheric variability which are not captured by the NA SLP EOF analysis. Computing an accurate DoE for the equatorial region would require to use different atmospheric variables and/or to extend the region where the SLP EOF are computed. Finally, the methodology used in this study could be used to infer the DoE in other mid-latitudes regions such as the Southern Ocean where the projected H_s changes due to anthropogenic climate change are expected to be the largest Hemer et al., 2013; Morim et al., 2019. Because the DoE depends on the ratio between the internal and forced variabilities, the DoE is expected to be sooner than the NA DoE in this region. However, our methodology relies on the strong relationship between the JFM H_s and SLP that has been demonstrated to hold in the NA in many studies. This relationship might not hold in every region and a detailed study of the SLP/H_s correlations should be performed before applying a similar methodology in a different region.

Data Availability Statement

ERA-5 data is available through Hersbach et al. (2020) and the CESM2 LENS2 data through Rodgers et al. (2021). ESA Sea State CCI data (Dodet et al., 2020) is available at http://dx.doi.org/10.5285/47140d618dcc40309e1edbca7e773478.

Acknowledgments
AH is funded by a CNRS-Region Bretagne Grant (Stratégie d'Attractivité Durable) CT N°LS 215643—REGION BRETAGNE (20006778). This research has also been partly funded by the European Space Agency as part of the Sea State CCI project of the Climate Change Initiative (CCI) (ESA ESRIN, contract no. 4000123651/18/I-NB).

References

Bacon, S., & Carter, D. J. T. (1993). A connection between mean wave height and atmospheric pressure gradient in the North Atlantic. *International Journal of Climatology*, *13*(4), 423–436. https://doi.org/10.1002/joc.3370130406

Casas-Prat, M., Wang, X. L., Mori, N., Feng, Y., Chan, R., & Shimura, T. (2022). Effects of internal climate variability on historical ocean wave height trend assessment. *Frontiers in Marine Science*, *9*. https://doi.org/10.3389/fmars.2022.847017

Castelle, B., Dodet, G., Masselink, G., & Scott, T. (2018). Increased winter-mean wave height, variability, and periodicity in the northeast Atlantic over 1949–2017. *Geophysical Research Letters*, *45*(8), 3586–3596. https://doi.org/10.1002/2017gl076884

Dee, D. P., Uppala, S. M., Simmons, A., Berrisford, P., Poli, P., Kobayashi, S., et al. (2011). The era-interim reanalysis: Configuration and performance of the data assimilation system. *Quarterly Journal of the Royal Meteorological Society*, *137*(656), 553–597. https://doi.org/10.1002/qj.828

Deser, C., Phillips, A., Bourdette, V., & Teng, H. (2012). Uncertainty in climate change projections: The role of internal variability. *Climate Dynamics*, *38*(3), 527–546. https://doi.org/10.1007/s00382-010-0977-x

Dobrynin, M., Murawski, J., Baehr, J., & Ilyina, T. (2015). Detection and attribution of climate change signal in ocean wind waves. *Journal of Climate*, *28*(4), 1578–1591. https://doi.org/10.1175/JCLI-D-13-00664.1

Dodet, G., Bertin, X., & Taborda, R. (2010). Wave climate variability in the North-East Atlantic Ocean over the last six decades. *Ocean Modelling*, *31*(3–4), 120–131. https://doi.org/10.1016/j.ocemod.2009.10.010

Dodet, G., Piolle, J.-F., Quilfen, Y., Abdalla, S., Accensi, M., Ardhuin, F., et al. (2020). The sea state CCI dataset v1: Towards a sea state climate data record based on satellite observations. *Earth System Science Data*, *12*(3), 1929–1951. https://doi.org/10.5194/essd-12-1929-2020

Erikson, L., Morim, J., Hemer, M., Young, I., Wang, X., Mentaschi, L., et al. (2022). Global ocean wave fields show consistent regional trends between 1980 and 2014 in a multi-product ensemble. *Communications Earth & Environment*, *3*(1), 320. https://doi.org/10.1038/s43247-022-00654-9

Giorgi, F., & Bi, X. (2009). Time of emergence (TOE) of GHG-forced precipitation change hot-spots. *Geophysical Research Letters*, *36*(6), L06709. https://doi.org/10.1029/2009GL037593

Gulev, S. K., Cotton, D., & Sterl, A. (1998). Intercomparison of the North Atlantic wave climatology from voluntary observing ships, satellite data and modelling. *Physics and Chemistry of the Earth*, *23*(5), 587–592. https://doi.org/10.1016/S0079-1946(98)00075-5

Hawkins, E., & Sutton, R. (2009). The potential to narrow uncertainty in regional climate predictions. *Bulletin of the American Meteorological Society*, *90*(8), 1095–1107. https://doi.org/10.1175/2009bams2607.1

Hawkins, E., & Sutton, R. (2011). The potential to narrow uncertainty in projections of regional precipitation change. *Climate Dynamics*, *37*(1), 407–418. https://doi.org/10.1007/s00382-010-0810-6

Hemer, M. A., Fan, Y., Mori, N., Semedo, A., & Wang, X. L. (2013). Projected changes in wave climate from a multi-model ensemble. *Nature Climate Change*, *3*(5), 471–476. https://doi.org/10.1038/nclimate1791

Hersbach, H., Bell, B., Berrisford, P., Hirahara, S., Horányi, A., Muñoz-Sabater, J., et al. (2020). The ERA5 global reanalysis. *Quarterly Journal of the Royal Meteorological Society*, *146*(730), 1999–2049. https://doi.org/10.1002/qj.3803

Hochet, A., Dodet, G., Ardhuin, F., Hemer, M. A., & Young, I. (2021). Sea state decadal variability in the North Atlantic: A review?

Kim, W. M., Yeager, S., Chang, P., & Danabasoglu, G. (2018). Low-frequency north Atlantic climate variability in the community Earth system model large ensemble. *Journal of Climate*, *31*(2), 787–813. https://doi.org/10.1175/jcli-d-17-0193.1

Kravtsov, S. (2017). Pronounced differences between observed and cmip5-simulated multidecadal climate variability in the twentieth century. *Geophysical Research Letters*, *44*(11), 5749–5757. https://doi.org/10.1002/2017gl074016

Kushnir, Y., Cardone, V., Greenwood, J., & Cane, M. (1997). The recent increase in north Atlantic wave heights. *Journal of Climate*, *10*(8), 2107–2113. https://doi.org/10.1175/1520-0442(1997)010<2107:triina>2.0.co;2

Lehner, F., Deser, C., Maher, N., Marotzke, J., Fischer, E. M., Brunner, L., et al. (2020). Partitioning climate projection uncertainty with multiple large ensembles and CMIP5/6. *Earth System Dynamics*, *11*(2), 491–508. https://doi.org/10.5194/esd-11-491-2020

Lemos, G., Semedo, A., Dobrynin, M., Behrens, A., Staneva, J., Bidlot, J.-R., & Miranda, P. M. (2019). Mid-twenty-first century global wave climate projections: Results from a dynamic CMIP5 based ensemble. *Global and Planetary Change*, *172*, 69–87. https://doi.org/10.1016/j.gloplacha.2018.09.011

Lemos, G., Semedo, A., Dobrynin, M., Menendez, M., & Miranda, P. M. A. (2020). Bias-corrected CMIP5-derived single-forcing future wind-wave climate projections toward the end of the twenty-first century. *Journal of Applied Meteorology and Climatology*, *59*(9), 1393–1414. https://doi.org/10.1175/JAMC-D-19-0297.1

Maher, N., Milinski, S., Suarez-Gutierrez, L., Botzet, M., Dobrynin, M., Kornblueh, L., et al. (2019). The Max Planck institute grand ensemble: Enabling the exploration of climate system variability. *Journal of Advances in Modeling Earth Systems*, *11*(7), 2050–2069. https://doi.org/10.1029/2019MS001639

Masson-Delmotte, V., Zhai, P., Pirani, A., Connors, C., Péan, C., Berger, S., et al. (2021). [Book section]. In *Climate change 2021: The physical science basis. Contribution of working group I to the sixth assessment report of the intergovernmental panel on climate change*. Cambridge University Press.

Mizuta, R., Murata, A., Ishii, M., Shiogama, H., Hibino, K., Mori, N., et al. (2017). Over 5,000 years of ensemble future climate simulations by 60-km global and 20-km regional atmospheric models. *Bulletin of the American Meteorological Society*, *98*(7), 1383–1398. https://doi.org/10.1175/bams-d-16-0099.1

Morim, J., Hemer, M., Wang, X. L., Cartwright, N., Trenham, C., Semedo, A., et al. (2019). Robustness and uncertainties in global multivariate wind-wave climate projections. *Nature Climate Change*, *9*(9), 711–718. https://doi.org/10.1038/s41558-019-0542-5

Nguyen, T.-H., Min, S.-K., Paik, S., & Lee, D. (2018). Time of emergence in regional precipitation changes: An updated assessment using the CMIP5 multi-model ensemble. *Climate Dynamics*, *51*(9), 3179–3193. https://doi.org/10.1007/s00382-018-4073-y

Piollé, J.-F., Dodet, G., & Quilfen, Y. (2020). *ESA sea state climate change initiative (Sea_state_cci): Global remote sensing merged multi-mission monthly gridded significant wave height, L4 product, version 1.1*. Centre for Environmental Data Analysis. https://doi.org/10.5285/47140d618dcc40309e1edbca7e773478

Ribal, A., & Young, I. R. (2019). 33 years of globally calibrated wave height and wind speed data based on altimeter observations. *Scientific Data*, *6*(1), 1–15. https://doi.org/10.1038/s41597-019-0083-9

Rodgers, K. B., Lee, S.-S., Rosenbloom, N., Timmermann, A., Danabasoglu, G., Deser, C., et al. (2021). Ubiquity of human-induced changes in climate variability. *Earth System Dynamics*, *12*(4), 1393–1411. https://doi.org/10.5194/esd-12-1393-2021

Sévellec, F., & Drijfhout, S. S. (2019). The signal-to-noise paradox for interannual surface atmospheric temperature predictions. *Geophysical Research Letters*, *46*(15), 9031–9041. https://doi.org/10.1029/2019GL083855

Shimura, T., Mori, N., & Mase, H. (2013). Ocean waves and teleconnection patterns in the northern hemisphere. *Journal of Climate*, *26*(21), 8654–8670. https://doi.org/10.1175/JCLI-D-12-00397.1

Simpson, I. R., Deser, C., McKinnon, K. A., & Barnes, E. A. (2018). Modeled and observed multidecadal variability in the north Atlantic jet stream and its connection to sea surface temperatures. *Journal of Climate*, *31*(20), 8313–8338. https://doi.org/10.1175/jcli-d-18-0168.1

Suckling, E. B., van Oldenborgh, G. J., Eden, J. M., & Hawkins, E. (2017). An empirical model for probabilistic decadal prediction: Global attribution and regional hindcasts. *Journal of Climate*, *48*(9–10), 3115–3138. https://doi.org/10.1007/s00382-016-3255-8

Timmermans, B. W., Gommenginger, C. P., Dodet, G., & Bidlot, J.-R. (2020). Global wave height trends and variability from new multimission satellite altimeter products, reanalyses, and wave buoys. *Geophysical Research Letters*, *47*(9), e2019GL086880. https://doi.org/10.1029/2019GL086880

Trigo, R. M., Valente, M. A., Trigo, I. F., Miranda, P. M. A., Ramos, A. M., Paredes, D., & García-Herrera, R. (2008). The impact of north Atlantic wind and cyclone trends on European precipitation and significant wave height in the Atlantic. *Annals of the New York Academy of Sciences*, *1146*(1), 212–234. https://doi.org/10.1196/annals.1446.014

Wang, X. L., Feng, Y., & Swail, V. (2012). North Atlantic wave height trends as reconstructed from the 20th century reanalysis. *Geophysical Research Letters*, *39*(18), L18705. https://doi.org/10.1029/2012gl053381

WMO. (2015). Guide to climatological practices (WMO-100). (Technical Report). Retrieved from https://public.wmo.int/en/resources/library/guide-climatological-practices-wmo-100

Woolf, D. K. (2002). Variability and predictability of the North Atlantic wave climate. *Journal of Geophysical Research*, *107*(C10), 3145. https://doi.org/10.1029/2001JC001124

Young, I. R., & Ribal, A. (2019). Multiplatform evaluation of global trends in wind speed and wave height. *Science*, *364*(6440), 548–552. https://doi.org/10.1126/science.aav9527

Young, I. R., Zieger, S., & Babanin, A. V. (2011). Global trends in wind speed and wave height. *Science*, *332*(6028), 451–455. https://doi.org/10.1126/science.1197219

References From the Supporting Information

Bricheno, L. M., & Wolf, J. (2018). Future wave conditions of Europe, in response to high-end climate change scenarios. *Journal of Geophysical Research: Oceans*, *123*(12), 8762–8791. https://doi.org/10.1029/2018jc013866

Hurrell, J., & Staff, N. (2020). The climate data guide: Hurrell North Atlantic oscillation (NAO) index (station-based). Retrieved from https://climatedataguide.ucar.edu/climate-data/hurrell-north-atlantic-oscillation-nao-index-station-based

Mentaschi, L., Vousdoukas, M. I., Voukouvalas, E., Dosio, A., & Feyen, L. (2017). Global changes of extreme coastal wave energy fluxes triggered by intensified teleconnection patterns. *Geophysical Research Letters*, *44*(5), 2416–2426. https://doi.org/10.1002/2016gl072488

Reguero, B., Menéndez, M., Méndez, F., Mínguez, R., & Losada, I. (2012). A global ocean wave (GOW) calibrated reanalysis from 1948 onwards. *Coastal Engineering*, *65*, 38–55. https://doi.org/10.1016/j.coastaleng.2012.03.003

Sharmar, V. D., Markina, M. Y., & Gulev, S. K. (2021). Global ocean wind-wave model hindcasts forced by different reanalyzes: A comparative assessment. *Journal of Geophysical Research: Oceans*, *126*(1), e2020JC016710. https://doi.org/10.1029/2020JC016710

Smith, G. A., Hemer, M., Greenslade, D., Trenham, C., Zieger, S., & Durrant, T. (2021). Global wave hindcast with Australian and Pacific island focus: From past to present. *Geoscience Data Journal*, *8*(1), 24–33. https://doi.org/10.1002/gdj3.104

Stopa, J. E., Ardhuin, F., Babanin, A., & Zieger, S. (2016). Comparison and validation of physical wave parameterizations in spectral wave models. *Ocean Modelling*, *103*, 2–17. https://doi.org/10.1016/j.ocemod.2015.09.003